HHS Public Access

Author manuscript

Magn Reson Med. Author manuscript; available in PMC 2018 April 01.

Published in final edited form as:

Magn Reson Med. 2017 April ; 77(4): 1713–1727. doi:10.1002/mrm.26227.

Mitigation of Partial-Volume Effects in Susceptibility-Based Oxygenation Measurements by Joint Utilization of Magnitude and Phase (JUMP)

Patrick McDaniel[1], **Berkin Bilgic**[2], **Audrey Fan**[3], **Jeffrey Stout**[4], and **Elfar Adalsteinsson**[1,4]

[1]Dept of Electrical Engineering and Computer Science, Massachusetts Institute of Technology, Cambridge, MA, USA

[2]A. A. Martinos Center for Biomedical Imaging, Dept of Radiology, Massachusetts General Hospital, Charlestown, MA, USA

[3]Richard M. Lucas Center for Imaging, Stanford University, Stanford, CA, USA

[4]Harvard-MIT Division of Health Sciences and Technology, Cambridge, MA, USA

Abstract

Purpose—Susceptibility-based blood oxygenation measurements in small vessels of the brain derive from GRE phase, and can provide localized assessment of brain function and pathology. However, when vessel diameter becomes smaller than the acquisition voxel size, partial-volume effects compromise these measurements. In this study, a technique is proposed to improve the reliability of vessel oxygenation estimates in the presence of partial-volume effects.

Methods—Intravoxel susceptibility variations are present when a vessel and parenchyma experience partial-volume effects, modifying the voxel's GRE phase signal and attenuating the GRE magnitude signal. By Joint Utilization of Magnitude and Phase (JUMP), both vessel susceptibility and voxel partial-volume fraction can be estimated, providing measurements of venous oxygen saturation (Y_v) in straight, nearly-vertical vessels that have improved robustness to partial-volume effects.

Results—JUMP is demonstrated by estimating vessel Y_v in numerical and *in vivo* experiments. Deviations from ground truth of Y_v measurements in vessels tilted up to 30° from B_0 were reduced by over 50% when using JUMP compared to when using phase-only techniques.

Conclusion—JUMP exploits both magnitude and phase data in GRE imaging to mitigate partial-volume effects in estimation of vessel oxygenation

Corresponding author: Patrick McDaniel, patmcd@mit.edu, Office 36-776, 77 Massachusetts Avenue, Massachusetts Institute of Technology, Cambridge, MA 02139.

Supporting File Information

Below is a list of the files uploaded as Supporting Information

(a) <mrm_JUMP_app_figs_supporting_r3s1.docx> - File containing supporting appendices, figures, and tables. Intended for online publication

Keywords

Susceptibility-weighted imaging; Oxygenation; Partial-volume effects; Quantitative Susceptibility Mapping

Introduction

Accurate, quantitative, *in vivo* measurements of brain oxygenation have many clinical and scientific applications, including identification of penumbra during ischemic injury (1), monitoring of cancer therapy (2), and calculation of the cerebral metabolic rate of oxygen ($CMRO_2$) (3). Several techniques have been developed to obtain venous oxygen saturation (Y_v) measurements non-invasively using MRI. These include quantitative BOLD (4) and QUIXOTIC (5) for microvasculature measurements; MRI susceptometry (6) and Quantitative Susceptibility Mapping (QSM) (7) for local macrovasculature measurements; and TRUST (8) for global measurements in large, draining veins. In particular, susceptibility-based techniques such as QSM and MRI susceptometry have been used for Y_v assessment in many clinical and pre-clinical studies (9–14), and qualitative Susceptibility-Weighted Imaging (SWI) has found increasing clinical usage to evaluate oxygenation based on vessel contrast (1,15). Susceptibility-based techniques are relatively easy to adopt in the clinic, as they derive from the phase of a gradient-echo acquisition.

Y_v estimation from susceptibility requires the isolation of pure venous blood signal from a vascular structure. Whole-brain Y_v techniques can reliably isolate blood signal from large draining veins, but these do not provide regional Y_v information that would be important for functional or pathological assessment. We are interested measuring Y_v in smaller vessels, as they reflect local physiology. However, studies measuring Y_v in small vessels by MRI susceptometry and QSM suffer from partial-volume effects between veins and parenchyma (11,13,14). This excludes many visible venous voxels from QSM analysis, limiting both the number of data points that can be analyzed for a given blood vessel, and the minimum radius of blood vessels that can be analyzed. In susceptibility-based imaging, it has been observed that partial-volume effects between veins and parenchyma lead to attenuation of the magnitude signal (16), a fact which is exploited in clinical SWI (15). However, a proper treatment of and correction for partial-volume effects in QSM oxygenation measurements is currently lacking.

We propose a novel technique utilizing both the magnitude and phase of the GRE acquisition to mitigate partial-volume effects in Y_v measurements. We call this Joint Utilization of Magnitude and Phase (JUMP). Prior studies utilize only the signal phase (QSM, MRI susceptometry) or signal magnitude (qBOLD, TRUST), for Y_v estimation, and thus only have a single measurement per voxel. This single measurement does not provide enough information to characterize both partial-volume fraction and Y_v. However, the full complex GRE signal provides two measurements from the acquisition – magnitude and phase - which together provide sufficient information to estimate both Y_v and the degree of partial-voluming if a vein can be modeled as a long, straight cylinder.

QSM techniques have employed the GRE magnitude image as a structural prior to aid in solution of the underdetermined dipole inversion problem (7,17). However, these optimization techniques utilize the phase image alone to enforce data consistency, and thus suffer from partial-volume effects. Joint use of the magnitude and phase signals has been applied to GRE data for tractography by calculating the eigenvectors shared by the R_2^* and susceptibility tensors (18), and to reduce banding artifacts due to B_0 inhomogeneity in balanced steady-state free procession (bSSFP) images (19).

In this work, we describe JUMP and demonstrate its efficacy to estimate venous susceptibility values and Y_v from vessels that are nearly parallel to the main magnetic field. JUMP is compared to traditional MRI susceptometry and QSM-based measurements of Y_v from simulated and *in vivo* experiments acquired at different image resolutions.

Theory

Oxygen Saturation and Magnetic Susceptibility

Hemoglobin in blood is strongly paramagnetic relative to water when in the deoxygenated state (20). In whole blood, this can be expressed as a relationship between its magnetic susceptibility $\Delta\chi$ and its absolute fractional hemoglobin oxygen saturation, Y_v:

$$\Delta\chi = \chi_{do} \cdot Hct \cdot (1 - Y_v) \quad (1)$$

χ_{do} is the susceptibility difference between fully oxygenated and fully deoxygenated red blood cells, and is taken to be 0.27 *ppm* (cgs) (9, 21). The blood hematocrit, *Hct*, is taken to be 0.38 for females and 0.42 for males (3,22). Our goal is to use MRI signals to measure the susceptibility shift in a vein (relative to water) and quantify its Y_v through the linear relationship in Eq. 1.

Susceptibility-Induced Field Variations

An object with non-zero magnetic susceptibility relative to water ($\Delta\chi$), when placed in a magnetic field B_0, will generate a spatially-varying magnetic field pattern that can be observed with MRI. For a general vessel with arbitrary orientation and geometry, this field perturbation has a complex relationship with the underlying susceptibility distribution that is determined by the intrinsic dipole imaging kernel.

If a straight blood vessel is modeled as a long parallel cylinder, however, the estimation of susceptibility inside the vein is simplified and Eq. 1 can then be used for Y_v quantification (16). For a long, cylindrical object with susceptibility $\Delta\chi$ oriented with its longitudinal axis at an angle θ to B_0, the induced field inside the cylinder, $\Delta B_{0,cyl}$, will be:

$$\Delta B_{0,cyl} = |B_0| \cdot 4\pi\Delta\chi \cdot \frac{(3\cos^2\theta - 1)}{6} \quad (2)$$

The field outside the cylinder, B_{out}, will be:

$$\Delta B_{0,out} = |B_0| \cdot 4\pi\Delta\chi \cdot \frac{1}{2}\left(\frac{R}{r}\right)^2 \cos 2\phi \sin^2\theta \quad (3)$$

Here, R is the radius of the cylinder, r is the distance from the cylinder's axis, and ϕ is the azimuthal angle about the cylinder (23). Since this term is proportional to $\sin^2\theta$, it is small for small tilt angles θ between the vessel and B_0. For this reason, we will assume that $\Delta B_{0,out} = 0$, which removes any dependence on the parameters r, R, and ϕ.

Partial-Volume Effects and GRE Signal

Suppose we overlay a grid on an in-plane vessel where the cells represent the voxels of a GRE acquisition (Figure 1a). For small vessels, many voxels/grid cells that intersect the vessel will contain compartments of both vein and parenchyma – i.e. they suffer from partial-volume effects (Figure 1b). Assuming linear phase evolution with time, the phase in each compartment is equal to:

$$\Delta\varphi_{cyl/out} = \Delta B_{0,cyl/out} \cdot 2\pi\gamma \cdot TE \quad (4)$$

We can then use a complex signal addition model akin to Dixon methods (24) to describe how the measured complex voxel signal depends on the tissue parameters and the partial-volume fraction α (Figure 1c–1f). For a given voxel, α represents the fraction of that voxel's signal that originates in the blood vessel compartment, which is not necessarily the physical fraction of the ideal, rectangular voxel that consists of blood. This is because of the sinc spatial voxel function associated with an MRI acquisition, where $\mathrm{sinc}(x) = \sin(\pi x)/(\pi x)$.

As a consequence, α is given by a convolution between a sinc function (representing the voxel) and a shifted rect function (representing blood vessel position). For particular vessel sizes and positions, α can be either larger than 1 or less than 0. This illustrated in two simplified 1D cases in Figure 1g, where $\alpha > 1$, and 1h, where $\alpha < 0$. For this study, it was assumed that $\alpha \in [-0.16, 1.39]$, as detailed in the Appendix section *Partial-Volume Fraction* α. Voxels with negative α necessarily have less than 16% signal contribution from blood, and are immediately adjacent to a voxel with larger, positive α, as illustrated in Figure 1i. As a consequence, we do not consider such voxels in the remainder of this work, as we can always use an adjacent voxel with much larger signal.

Using the parameters in Table 1, we find that the measured voxel magnitude and phase are equal to:

$$M_{vox} = \sqrt{\alpha^2 M_b^2 + (1-\alpha)^2 M_a^2 + 2\alpha(1-\alpha) M_a M_b \cos(\varphi_b - \varphi_a)} \quad (5)$$

$$\varphi_{vox}=\varphi_a+\tan^{-1}\left[\frac{\sin(\varphi_b-\varphi_a)\,M_b\alpha}{\cos(\varphi_b-\varphi_a)\,M_b\alpha+M_a(1-\alpha)}\right] \quad (6)$$

$$\varphi_b=\Delta\varphi_{cyl}(Y_v,\theta,TE)=2\pi\gamma\cdot TE\cdot|B_0|\cdot 4\pi\Delta\chi\cdot\frac{(3\cos^2\theta-1)}{6} \quad (7)$$

We assume extravascular magnetic field equals 0. Further, susceptibilities of gray matter, white matter, and CSF are an order of magnitude lower than typical venous blood susceptibilities (25–27) and are comparable to the oxyhemoglobin susceptibility, which is typically ignored (28). Thus, we make the approximation that phase in the parenchyma φ_a = 0.

M_a and M_b are the magnitude signal intensities for parenchyma and venous blood, respectively, for voxels without partial-volume effects. We assume M_a and M_b both undergo monoexponential T_2^* decay.

For parenchyma:

$$M_a(TE)=K\cdot 0.0721\cdot e^{-TE/66.0ms} \quad (8)$$

And for blood:

$$M_b(TE,Y_v)=K\cdot 0.0786\cdot e^{-(TE\cdot R_2^*(Y_v))} \quad (9)$$

$$R_2^*(Y_v)=17.5+39.1\cdot(1-Y_v)+119\cdot(1-Y_v)^2 \quad (10)$$

The derivation of Eqs. (8–10) is given in the Supporting Appendix section *Tissue GRE Signal Magnitude*. The constant K describes the absolute signal intensity, and varies slowly across an image (29). Since our magnitude signal measurements M_{vox} are in absolute scanner units, we include the absolute signal intensity K as an unknown parameter. K is calculated from a gray matter ROI near each vessel at each TE (Figure 4b). This measurement is potentially affected by CSF contamination (30) and by vascular microstructure variations in gray matter (31). However, these effects are expected to be small in JUMP, and are ignored (see Appendix sections *CSF Contamination in Gray Matter Voxels* and *Gray Matter Magnitude Signal Estimation*).

The calculation of blood phase in the signal model requires knowledge of the vessel tilt angle θ with respect to B_0 (Eq. 7). This angle is determined by fitting the set of voxel coordinates along the centerline of the vein of interest to a line.

Parameter Estimation from Signal Magnitude and Phase

The two-compartment signal model is described by Eqs. 1 and 5–10 and the parameters in Table 1. The goal of JUMP is to calculate Y_V and α for a voxel given M_{VOX} and φ_{VOX}. Figure 2 shows M_{VOX} and φ_{VOX}, for all possible choices of α and Y_V at TE of 8.1ms, 14.2ms, and 20.3ms at $\theta = 20°$. The dashed curves illustrate how a given measurement of M_{VOX} determines a particular contour in (α, Y_V)-space. Likewise, the solid curves show how a measurement of φ_{VOX} specifies a different locus of such points. The intersection of these sets is, in general, a single point ($\hat{\alpha}$, $\hat{Y}_V$), so that a single complex signal measurement (φ_{VOX}, M_{VOX}) provides enough information to determine both the partial-volume fraction and the phase inside the vein. Due to the form of Eqs. 1 and 5–10, there are no analytical expressions for $\hat{\alpha}$ and $\hat{Y}_V$ in terms of other parameters. Therefore, we solve for $\hat{\alpha}$ and $\hat{Y}_V$ with the following least-squares minimization problem:

$$\min_{\hat{\alpha},\hat{Y}_v} \left[\sum_i \| \hat{M}_{v,i}(\hat{\alpha},\hat{Y}_v) \cdot e^{j\hat{\varphi}_{v,i}(\hat{\alpha},\hat{Y}_v)} - M_{v,i} \cdot e^{j\varphi_{v,i}} \|^2 \right] \quad (11)$$

where the i index indicates the i-th echo time. This minimization problem requires the measured complex signal vectors at each echo time ($M_{v,i}$, $\varphi_{v,i}$) to match those predicted by the model ($\hat{M}_{v,i}$ and $\hat{\varphi}_{v,i}$), and uses the sum of the ℓ_2 norms of the complex residuals as a cost function. The least-squares formulation allows for complex data from multiple echoes to be simultaneously used to solve for $\hat{\alpha}$ and $\hat{Y}_V$. For the solution to Eq. 11 to be physically meaningful, we require: $\hat{Y}_V \in [0,1]$ and $\hat{\alpha} \in [-0.163, 1.39]$. The range of acceptable $\hat{\alpha}$ derives from the sinc-shaped voxel functions inherent in the MRI acquisitions and the assumption that blood vessels are 1D cylinders. A detailed analysis of α is found in the Supporting Appendix section *Partial-Volume Fraction α*. Solutions of Eq. 11 that fall on the corners of the $\hat{Y}_V$ - $\hat{\alpha}$ range are assumed to be unreliable and are discarded.

It is also possible with JUMP to obtain a single measurement of $\hat{Y}_V$ for a vessel as opposed to a separate $\hat{Y}_V$ measurement for each voxel. This is done by modifying the minimization problem in Eq. 11 to minimize the sum of the residuals from all voxels simultaneously while requiring that $\hat{Y}_V$ be the same for each voxel:

$$\min_{\{\hat{\alpha}_k\},\hat{Y}_v} \left[\sum_k \sum_i \| \hat{M}_{v,i}(\hat{\alpha}_k,\hat{Y}_v) \cdot e^{j\hat{\varphi}_{v,i}(\hat{\alpha}_k,\hat{Y}_v)} - M_{v,ik} \cdot e^{j\varphi_{v,ik}} \|^2 \right] \quad (12)$$

In this minimization, the sum over i adds the residuals at different TE, and the sum over k adds those from different voxels. $\{\hat{\alpha}_k\}$ represents the set of partial-volume fractions for all voxels. This approach, which we call Multi-Voxel JUMP (MV-JUMP) reduces the total

number of degrees of freedom in the optimization at the cost of ignoring variation in Y_V within a set of voxels.

In all cases, measured voxel phase is the signal phase at a particular value of TE, and not a difference in signal phase between multiple TEs. The distinction is important when partial-volume effects are present, as they cause nonlinear phase signal evolution with TE. This can be seen in Eqs 6 and 7, where blood phase (φ_b) evolves linearly with TE, but the measured voxel phase φ_{vox} does not linearly depend on φ_b.

Methods

Simulation Experiments – Numerical Vessels

Numerical vessels were created with a physiological range of six susceptibility values corresponding to Y_V values between 0.4 and 0.9, and were placed in a background with susceptibility equal to zero. The numerical vessels had a radius of 1.2mm, and were created at a resolution of 0.12mm isotropic. Vessels with tilt angle relative to B_0 of 0° to 40° were simulated in 10° increments. Vessels with offsets relative to the field of view of 0mm, 0.48mm, and 0.96mm were simulated by shifting the vessel location in the transverse plane. Corresponding magnitude intensity maps for the vessel and surrounding parenchyma were also created using Eqs. (8–10). The susceptibility maps were convolved with the dipole kernel (32,33) to generate ΔB_0 maps. Using the dipole kernel imposes a physically correct model on the system that does not assume the extravascular field, $\Delta B_{0,out}$, is equal to zero when calculating the magnetic field pattern induced by a susceptibility cylinder. Signal phase maps were then created by scaling the ΔB_0 maps via Eq. 4, assuming echo times (TE) of 8.1ms and 20.3ms and a B_0 field of 2.89 T. Using this phase map and the intensity maps, complex signal maps were generated. Complex Gaussian noise was then added such that the SNR of the simulated acquisitions matched the SNR of the *in vivo* acquisitions obtained in this study with a 32-channel surface coil (SNR = 20 at 0.6mm isotropic voxel size). Figure 3a shows the susceptibility, magnetization, and ΔB_0 map for vessel tilt angle of 20°.

Low-resolution acquisitions with 18 voxel sizes between 0.49mm and 6.00mm isotropic were simulated by truncating the high-resolution k-space data to the appropriate size and applying an inverse DFT. Figure 3b shows example simulated low-resolution magnitude and phase images acquired at 2.6mm, 1.1mm, and 0.7mm isotropic voxel sizes. Vessel ROI masks were manually identified from the low-resolution acquisitions and analyzed with the processing pipeline (described below). Example vessel ROI masks are shown in Figure 3b.

For each vessel and acquisition, ground truth α-maps and JUMP-estimated $\hat{\alpha}$-maps were created. Maps of extravascular magnetic field were also created to analyze the effects of vessel susceptibility on parenchyma field offset.

Simulation Experiments – Retrospective Analysis of *in vivo* Data

Previously-published *in vivo* GRE data were analyzed (28). These acquisitions had a native resolution of 0.6 × 0.6 × 0.6mm^3, and were numerically cropped in k-space to simulate acquisitions with voxel sizes of 1.2 × 1.2 × 1.2 mm^3, 1.8 × 1.8 × 1.8 mm^3, and 2.4 × 2.4 × 2.4mm^3. A single pial vessel was identified for analysis.

In vivo Experiments

Four subjects (2 male, 2 female) were scanned with IRB approval on a 3T Siemens Trio system. Flow-compensated GRE images were acquired at five resolutions: 0.6 × 0.6 × 0.6 mm^3, 0.7 × 0.7 × 0.8mm^3, 0.9 × 0.9 × 1.0mm^3, 1.2 × 1.2 × 1.5mm^3, and 1.8 × 1.8 × 1.8 mm^2. Sequence parameters for all acquisitions were: TR = 30ms; TE = 8.1ms, 20.3ms; flip angle = 15°; SENSE acceleration factor R=2 × 2; bandwidth = 260Hz/pixel; field of view = 224 × 189 × 144mm^3. Acquisition times varied between 10m23s (0.6 × 0.6 × 0.6 mm^3) to 1m21s (1.8 × 1.8 × 1.8mm^3), and matrix sizes varied from 384 × 324 × 240 to 128 × 108 × 80. Data were acquired with the product 32-channel head coil, and individual coil data were saved for all acquisitions.

Separate low-resolution GRE acquisitions were acquired for coil sensitivity estimation with the following parameters: TR = 4ms; TE = 1.68ms; flip angle = 5°; bandwidth = 1000Hz/pixel; resolution = 1.8 × 3.0 × 3.0mm^3; field of view = 224 × 189 × 144mm^3; acquisition time (TA) = 16s. Data were acquired with the product 32-channel head coil and with the body coil, and individual coil data were saved. SNR was not explicitly matched between different-resolution acquisitions, and a single average was acquired for each resolution.

Reconstruction and coil data combination was performed with ESPIRiT/SENSE using the Berkeley Advanced Reconstruction Toolbox (34). Brain masks for further analysis were created from the reconstructed magnitude images using FSL BET (35). Phase images were unwrapped with the Robust Unwrap algorithm (36). Background field removal was performed with SHARP (37) using the Fast QSM Magnitude Toolbox (38). Figure 4a shows sagittal sections of representative magnitude and SHARP phase images for all resolutions, respectively.

Processing Pipeline

Data from numerical simulations and *in vivo* experiments were analyzed with the same pipeline. Unwrapped phase maps with background variations removed were processed with the Fast QSM Magnitude Toolbox to generate L1-regularized susceptibility maps. ROI masks for nearly-vertical veins were then manually identified from susceptibility maps and SHARP phase maps at all resolutions (Figure 4a). To estimate vessel tilt angle, these masks were fit to a line in 3D with least-squares. Baseline magnitude signal intensity was estimated from the average signal in a gray matter ROI adjacent to each vessel (Figure 4b). The ROI consisted of rectangular regions in the axial and coronal planes of at least 6mm and 10mm in length, respectively. The tissue ROI was selected to exclude any voxels that visibly contained large blood vessels. To enable comparisons with other SvO_2 quantification techniques, OEF was estimated in four ways:

1. JUMP was performed to estimate $\hat{\alpha}$ and $\hat{Y}_V$ from Eqs 11. The average and variance of $\hat{Y}_V$ across all voxels in a vessel were obtained,
2. MV-JUMP was performed to estimate $\hat{\alpha}$ for each voxel and $\hat{Y}_V$ for the whole vessel from Eq. 12,
3. Y_V was also measured using direct measurement from an L1-regularized QSM map, and

4. Direct measurement from a SHARP phase map using MRI susceptometry (16).

For both JUMP and MV-JUMP, the nonlinear inverse problems in Eqs. 11 and 12 were solved using the MATALB fmincon function with an initial guesses for $\hat{\alpha}$ and $\hat{Y}_V$ of 0.4 and 0.6. For JUMP, we imposed the constraints: $\hat{\alpha} \in [0.2, 1.3]$ and $\hat{Y}_V \in [0.2, 0.99]$, and for MV-JUMP, we required that: $\hat{\alpha} \in [-0.1, 1.3]$ and $\hat{Y}_V \in [0.2, 0.99]$. For the L1-regularized QSM and MRI susceptometry methods, the single voxel with the highest average signal from both TEs within in the vessel ROI was used. Vessel diameter was visually estimated in order to normalize the acquisition voxel sizes to vessel size.

For the numerical and *in vivo* acquisitions, JUMP and MV-JUMP $\hat{\alpha}$-maps were created.

Results

Effects of Background Removal on Phase Signal

The effect of the processing pipeline on the underlying vessel phase signal was assessed. In one subject, two vessels were analyzed at three different stages of processing:

1. As raw phase data (unprocessed, wrapped phase)
2. As unwrapped phase data with no background phase removal performed
3. As background-removal-processed (SHARP-processed), unwrapped phase data

Three voxels in each vessel were identified. For each voxel, its phase signals relative to the voxels immediately anterior and immediately posterior were calculated, as illustrated in Supporting Figure S1. The average of these phase signals is assumed to accurately reflect the voxel signal, since it removes zeroth- and first- order variations in background phase across the brain. The processing pipeline, including phase unwrapping and SHARP background removal, introduced less than 0.03% error to the individual voxel signals.

Simulation Experiments – Numerical Vessels

Figure 5a and 5b show the estimated $\hat{Y}_V$ from a vessel with known Y_V of 0.7 and tilt angle of 20° for different acquisition voxel sizes using all four techniques: JUMP, MV-JUMP, QSM, and MRI susceptometry. The estimated vessel $\hat{Y}_V$ was always between 0.64 and 0.70 using JUMP, and between 0.66 and 0.70 using MV-JUMP, for voxel sizes up to 2x the vessel diameter. The estimates obtained with QSM and MRI susceptometry were between 0.65 and 0.70 for a voxel size of 0.7x the vessel diameter. Partial volume effects, however, led to overestimation or underestimation of OEF by QSM and MRI susceptibility, depending on acquisition resolution. For all combinations of vessel angle up to 30° and acquisition resolution up to 1.5x vessel diameter, the variation in $\hat{Y}_V$ across acquisition resolution was, for both JUMP and MV-JUMP, less than half of that obtained with either MRI susceptometry or QSM.

Figures 5c and 5d show JUMP and MV-JUMP estimates of $\hat{Y}_V$ from vessels with six different ground truth Y_V values oriented at five different angles to B_0, obtained with TE={8.1ms, 20.3ms}. Each sub-plot shows $\hat{Y}_V$ estimates obtained with all three techniques for a given choice of ground truth Y_V and vessel angle. Subplots that are shaded in Figure 5d

have JUMP $\hat{Y}_V$ estimates that deviate less than 0.12 from ground truth up for all resolutions up to 1.5x vessel diameter. For acquisition resolutions less than 1.5x the vessel diameter, vessel tilt angles up to 30° from B_0 and true vessel Y_V of 0.6 and greater, the JUMP- and MV-JUMP-estimated $\hat{Y}_V$ were within 0.10 (absolute oxygenation fraction) of ground truth. For the same acquisition resolutions and vessel tilt angles, and with Y_V down to 0.4, JUMP obtained $\hat{Y}_V$ estimates that were within 0.12 of ground truth, and MV-JUMP obtained $\hat{Y}_V$ estimates within 0.19 of ground truth. Under the same conditions, QSM and MRI susceptometry produced $\hat{Y}_V$ measurements that deviated from ground truth by up to 0.23 and 0.32, respectively, for vessels with Y_V down to 0.6. For vessels with Y_V down to 0.4, the errors were up to 0.47 and 0.54, respectively.

For the case where tilt angle is 20° and Y_V is 0.6, the RMSE across voxel size of JUMP $\hat{Y}_V$ estimates from ground truth is 0.032, while the RMSE of MV-JUMP $\hat{Y}_V$ is 0.028, a 13% reduction. When tilt angle is 20° and Y_V is 0.9, the JUMP $\hat{Y}_V$ RMSE is 0.052 and the MV-JUMP $\hat{Y}_V$ RMSE is 0.033, a 37% reduction. All RMSEs were calculated for voxels up to 1.5x vessel diameter, and accounted for non-uniform sampling across voxel size.

Supporting figures highlight additional simulations:

1. Supporting Figures S2a and S2b show that $\hat{Y}_V$ estimates obtained using JUMP and MV-JUMP are similar for vessels situated at different sub-voxel offsets relative to the field of view.
2. Supporting Figures S3a and S3b show corresponding correlation plots between ground truth and JUMP-estimated $\hat{\alpha}$-maps for each vessel. For $Y_V = 0.9$, MV-JUMP has 38% lower RMSE than JUMP at a 0.7mm voxel size, and 39% lower at a 1.1mm voxel size. For $Y_V = 0.6$, MV-JUMP outperforms JUMP by 18% at 0.7mm voxel size, and by 9.2% at 1.1mm voxel size.
3. Supporting Figures S4 and S5 summarize the extravascular magnetic fields produced by the blood vessels. For 0.7mm isotropic voxel size and $Y_V = 0.4$, a positive phase shift was observed in the parenchyma compartment of voxels immediately above and below the vessel. For a 2.6mm voxel size and $Y_V = 0.4$, a negative phase shift was observed in the parenchyma compartment of vessel-containing voxels.
4. Supporting Figure S6 summarizes JUMP and MV-JUMP $\hat{Y}_V$ estimates obtained when assuming gray matter R_2^* was different from ground truth, and shows that JUMP is robust to 10% variations in gray matter magnitude intensity. Details are described in the Supporting Appendix section *Gray Matter Magnitude Signal Estimation*.

Simulation Experiments – Retrospective Analysis of *in vivo* Data

A pial vein analyzed by retrospective undersampling of *in vivo* data is shown in Figure 6. JUMP $\hat{Y}_V$-measurements varied between 0.53 and 0.58 and MV-JUMP $\hat{Y}_V$ measurements varied between 0.56 and 0.63 as voxel size varies. For comparison, QSM and MRI susceptometry measurements varied from 0.52 to 0.96 and 0.58 to 0.95, respectively. Thus, JUMP and MV-JUMP saw smaller variations in $\hat{Y}_V$ than the other two methods.

In vivo Experiments

Figure 7a shows representative phase and susceptibility map maximum intensity projections from subject 4. Five veins were identified in the subject, and $\hat{Y}_V$ was determined by JUMP and MV-JUMP for different voxel sizes (Figure 7b). For voxel dimensions larger than the vessel diameter, direct measurement using QSM and MRI susceptometry yielded $\hat{Y}_V$ measurements with large errors. Table 2 summarizes individual vessel $\hat{Y}_V$ measurement ranges for all three techniques. For Subject 4, the range of JUMP $\hat{Y}_V$ estimates was 62% smaller than that of MRI susceptometry or QSM for all five veins, while for MV-JUMP the range was 61% smaller.

Figure 8 shows average $\hat{Y}_V$ for each subject (from five pial veins) at all acquisition resolutions. Table 2 summarizes across-vessel $\hat{Y}_V$ averages for each subject for all three techniques. Excepting subject 2, variation in MRI susceptometry and QSM $\hat{Y}_V$ measurements across voxel size was more than 2.5x the variation observed with JUMP. For subject 2, the variations with JUMP and MV-JUMP were under 78% that observed with the other two techniques. Note that for some vessels in the four subjects, MV-JUMP did not provide a valid $\hat{Y}_V$ solution at the lowest acquisition resolution, so those vessel $\hat{Y}_V$ ranges are for 4 resolutions instead of 5. Statistics that depend on such incomplete data are appended with an asterisk in Table 2.

Discussion

In both simulation and *in vivo* experiments, JUMP provides $\hat{Y}_V$ estimates in veins that are robust to changes in acquisition resolution and to partial-volume effects for voxel sizes up to 1.5x to 2x vessel diameter. $\hat{Y}_V$ measurements obtained with QSM or MRI susceptometry do not account for partial-volume effects, and are highly dependent on acquisition resolution. Thus, JUMP provides greater absolute $\hat{Y}_V$ measurement accuracy in small vessels. The background removal pipeline did not alter the phase signal of the blood vessels studied. In numerical experiments, neither vessel shift relative to the field of view, nor a 10% error in the presumed parenchyma intensity resulted in significant error.

By obtaining useful measurements from voxels that suffer from vein/parenchyma partial volume behavior, JUMP is able to accurately measure smaller blood vessels than QSM or MRI susceptometry. This fact also allows a greater number of voxels from a single blood vessel to be measured, and removes the need for manual identification of “reliable” voxels. This has two main consequences. The first is the elimination of artificial biases inherent in the manual identification of voxels without partial-voluming. The second is the ability to better quantify measurement uncertainty thanks to the larger number of data points per vessel. Both of these advantages mean that JUMP provides greater objectivity and quantifiable uncertainty in vessel $\hat{Y}_V$ measurements.

Two techniques, JUMP and MV-JUMP, were proposed and tested. MV-JUMP was observed to have 37% less RMSE in $\hat{Y}_V$ estimates and 38% less RMSE in $\hat{\alpha}$ estimates than JUMP in vessels with tilt angle of 20° and $Y_V = 0.9$.This may be because the MV-JUMP estimation problem has fewer degrees-of-freedom than the JUMP problem, and thus outperforms JUMP for high Y_V/low susceptibility. However, this possibility requires further study. With tilt

angle of 20° and Y_V = 0.6, JUMP and MV-JUMP provide closer RMSE in $\hat{Y}_V$ and $\hat{a}$ estimates. MV-JUMP required longer computation times for the same set of voxels than did JUMP due to the non-linear computational complexity of the MATLAB fmincon solver. JUMP and MV-JUMP both involve solving optimization problems to minimize the difference between the measured complex signal and the signal predicted from a model. Using the complex signal rather than only the phase means both JUMP and MV-JUMP are less sensitive to phase wrapping.

At voxel sizes smaller than 1x the vessel diameter, partial-volume effects were not expected to be a major problem. However, at these resolutions, MRI susceptometry and QSM sometimes underestimated vessel $\hat{Y}_V$ in numerical experiments, while JUMP did not show any such trend at smaller voxel sizes (eg. Figure 5a). This $\hat{Y}_V$ underestimation behavior of phase-only approaches may be a consequence of using only the single most intense voxel from each vessel. Selecting only a single voxel increases the effect of noise on the resulting measurement, since there is no averaging. This effect can be especially pronounced at smaller voxel sizes, where SNR is lower. By averaging across multiple voxels, this source of error is reduced in JUMP. One could likewise average across multiple voxels when using MRI susceptometry or QSM, but this would entail manually identifying voxels that lack partial-volume effects and would reduce the objectivity of the measurement.

In simulation, JUMP was less accurate for $\hat{Y}_V$ estimates at voxel sizes greater than 2x the vessel diameter. This is a natural consequence of limiting the minimum acceptable $\hat{a}$ value to 0.2 (i.e. a voxel whose side length is 2x the vessel diameter). For larger voxel sizes, the limit on acceptable $\hat{a}$ forbids JUMP from obtaining the correct solution. However, even for MV-JUMP, where we limited the minimum acceptable $\hat{a}$ to −0.1, voxels larger than 2x vessel diameter gave inaccurate $\hat{Y}_V$ estimates. This suggests that at such low resolutions, there is simply insufficient vessel signal in each voxel to make any accurate phase-based measurement of susceptibility. This error for voxel size greater than 2x vessel diameter may also be due to violation of the 2-compartment model at large voxel sizes.

In subject 2, several vessels could not be visibly identified in the phase image at 1.2mm and 1.8mm isotropic voxel size, which resulted in erroneous vessel $\hat{Y}_V$ measurements at these resolutions. This explains the large variation in 5-vessel average $\hat{Y}_V$ across acquisition resolution that was observed in subject 2.

JUMP is currently limited to relatively straight vessels parallel to the main field. In this work, all measured vessels had a tilt angle equal to or less than 30° to B_0. In experiments on numerical vessels, JUMP consistently underestimated $\hat{Y}_V$ in vessels oriented at 40° away from B_0. Several recent studies have utilized MRI susceptometry as a means of quantifying $\hat{Y}_V$ in such vertical vessels (3,9–14), and this work would be immediately relevant to such studies. Most vessels, however, do not meet these geometric specifications, and will not benefit from the current implementation of JUMP. The reasons for this dependence on vessel angle are twofold.

First, as vessel angle θ nears 54.7° – the “magic angle” – the intravascular field offset given in Eq. 2 nears zero. Thus, estimation of χ from ΔB_0 becomes an underdetermined problem.

Second, as θ nears 90°, the extravascular field perturbations given by Eq. 3 increase, and the approximation that $\Delta B_{0,out} = 0$ is invalidated. These effects are described in the Supporting Appendix section *Effects of Assuming* $\Delta B_{0,out} = 0$ *on Estimated* $\hat{Y}_v$.

Phase images in this study were processed using SHARP, which requires convolution of the brain-masked brain image with a spherical kernel. Since this convolution is not possible near the edge of the brain ROI, the brain mask is eroded by this spherical kernel to remove these unreliable voxels. As is particularly visible in Figure 6a, this reduces the field of view for vessel identification. Future work will examine background phase removal methods that do not suffer from this edge erosion problem.

In addition to obtaining an estimate of vessel oxygenation, JUMP provides estimates of partial-volume fraction for all voxels in an ROI. These estimates were observed to agree closely with the ground truth fractions for vessels tilted at 20° from B_0 (Supporting Figure S3), suggesting that JUMP and MV-JUMP can also obtain sub-voxel estimates of the sizes of structures. This is described further in the Supporting Appendix section *Partial-Volume Fraction* α.

Conclusion

We have demonstrated a method to obtain better accuracy in Y_v measurements from blood vessels oriented close to B_0. Accurate measurements can be obtained when the voxel size is up to 2x the vessel diameter and partial-volume effects are present. We further demonstrate that this technique can estimate the voxel signal fraction originating from blood.

Supplementary Material

Refer to Web version on PubMed Central for supplementary material.

Acknowledgments

This work was supported through NIH NIBIB: R01EB017337, P41-EB015896, 1U01MH093765, R00EB012107, R24MH106096, T32 EB001680 and the Stanford Neurosciences Institute Interdisciplinary Scholar Award.

References

1. Tong, Ka, Ashwal, S., Holshouser, Ba, Nickerson, JP., Wall, CJ., Shutter, La, Osterdock, RJ., Haacke, EM., Kido, D. Diffuse axonal injury in children: clinical correlation with hemorrhagic lesions. Ann Neurol. 2004; 56:36–50. DOI: 10.1002/ana.20123 [PubMed: 15236400]
2. Davda S, Bezabeh T. Advances in methods for assessing tumor hypoxia in vivo: Implications for treatment planning. Cancer Metastasis Rev. 2006; 25:469–480. DOI: 10.1007/s10555-006-9009-z [PubMed: 17029029]
3. Fan AP, Benner T, Bolar DS, Rosen BR, Adalsteinsson E. Phase-based regional oxygen metabolism (PROM) using MRI. Magn Reson Med. 2012; 67:669–678. DOI: 10.1002/mrm.23050 [PubMed: 21713981]
4. He X, Yablonskiy Da. Quantitative BOLD: mapping of human cerebral deoxygenated blood volume and oxygen extraction fraction: default state. Magn Reson Med. 2007; 57:115–26. DOI: 10.1002/mrm.21108 [PubMed: 17191227]

5. Bolar DS, Rosen BR, Sorensen aG, Adalsteinsson E. QUantitative Imaging of eXtraction of oxygen and TIssue consumption (QUIXOTIC) using venular-targeted velocity-selective spin labeling. Magn Reson Med. 2011; 66:1550–1562. DOI: 10.1002/mrm.22946 [PubMed: 21674615]
6. Weisskoff RM, Kiihne S. MRI Susceptometry: Image-Based Measurement. Magn Reson Med. 1992; 24:375–383. [PubMed: 1569876]
7. De Rochefort L, Liu T, Kressler B, Liu J, Spincemaille P, Lebon V, Wu J, Wang Y. Quantitative susceptibility map reconstruction from MR phase data using bayesian regularization: Validation and application to brain imaging. Magn Reson Med. 2010; 63:194–206. DOI: 10.1002/mrm.22187 [PubMed: 19953507]
8. Lu H, Ge Y. Quantitative evaluation of oxygenation in venous vessels using T2-Relaxation-Under-Spin-Tagging MRI. Magn Reson Med. 2008; 60:357–63. DOI: 10.1002/mrm.21627 [PubMed: 18666116]
9. Jain V, Langham MC, Wehrli FW. MRI estimation of global brain oxygen consumption rate. J Cereb Blood Flow Metab. 2010; 30:1598–607. DOI: 10.1038/jcbfm.2010.49 [PubMed: 20407465]
10. Rodgers ZB, Jain V, Englund EK, Langham MC, Wehrli FW. High temporal resolution MRI quantification of global cerebral metabolic rate of oxygen consumption in response to apneic challenge. J Cereb Blood Flow Metab. 2013; 33:1514–22. DOI: 10.1038/jcbfm.2013.110 [PubMed: 23838827]
11. Li M, Hu J, Miao Y, et al. In vivo measurement of oxygenation changes after stroke using susceptibility weighted imaging filtered phase data. PLoS One. 2013; 8:e63013.doi: 10.1371/journal.pone.0063013 [PubMed: 23675450]
12. Fujima N, Kudo K, Terae S, et al. Non-invasive measurement of oxygen saturation in the spinal vein using SWI: Quantitative evaluation under conditions of physiological and caffeine load. Neuroimage. 2011; 54:344–349. DOI: 10.1016/j.neuroimage.2010.08.020 [PubMed: 20727413]
13. Fan AP, Govindarajan ST, Kinkel RP, Madigan NK, Nielsen aS, Benner T, Tinelli E, Rosen BR, Adalsteinsson E, Mainero C. Quantitative oxygen extraction fraction from 7-Tesla MRI phase: reproducibility and application in multiple sclerosis. J Cereb Blood Flow Metab. 2014; :1–9. DOI: 10.1038/jcbfm.2014.187 [PubMed: 25352045]
14. Goodwin, Ja, Kudo, K., Shinohe, Y., Higuchi, S., Uwano, I., Yamashita, F., Sasaki, M. Susceptibility-Weighted Phase Imaging and Oxygen Extraction Fraction Measurement during Sedation and Sedation Recovery using 7T MRI. J Neuroimaging. 2014; doi: 10.1111/jon.12192
15. Haacke EM, Mittal S, Wu Z, Neelavalli J, Cheng Y-CN. Susceptibility-weighted imaging: technical aspects and clinical applications, part 1. AJNR Am J Neuroradiol. 2009; 30:19–30. DOI: 10.3174/ajnr.A1400 [PubMed: 19039041]
16. Haacke EM, Lai S, Reichenbach R, Hoogenraad FGC, Takeichi H, Lin W. In Vivo Measurement of Blood Oxygen Saturation Using Magnetic Resonance Imaging : A Direct Validation of the Blood Oxygen Level-Dependent Concept in Functional Brain Imaging. 1997; 346:341–346.
17. Liu J, Liu T, De Rochefort L, et al. Morphology enabled dipole inversion for quantitative susceptibility mapping using structural consistency between the magnitude image and the susceptibility map. Neuroimage. 2012; 59:2560–2568. DOI: 10.1016/j.neuroimage.2011.08.082 [PubMed: 21925276]
18. Dibb, R., Liu, C. Whole-Heart Myofiber Tractography Derived From Conjoint Relaxation and Susceptibility Tensor Imaging. International Society for Magnetic Resonance in Medicine; 2015; Toronto, Canada. 2015. p. 287
19. Xiang Q-S, Hoff MN. Banding artifact removal for bSSFP imaging with an elliptical signal model. Magn Reson Med. 2014; 71:927–33. DOI: 10.1002/mrm.25098 [PubMed: 24436006]
20. Wang Y, Liu T. Quantitative susceptibility mapping (QSM): Decoding MRI data for a tissue magnetic biomarker. Magn Reson Med. 2014; :n/a–n/a. DOI: 10.1002/mrm.25358
21. Spees WM, Yablonskiy DA, Oswood MC, Ackerman JJH. Water Proton MR Properties of Human Blood at 1.5 Tesla: Magnetic Susceptibility, T1, T2, T2*, and Non-Lorentzian Signal Behavior. 2001; 542:533–542.
22. Guyton, AC., Hall, JE. Red blood cells, anemia, and polycythemia. In: Guyton, AC., Hall, JE., editors. Textbook of medical physiology. 2000. p. 382-391.

23. Boxerman JL, Hamberg LM, Rosen BR, Weisskoff RM. MR contrast due to intravascular magnetic susceptibility perturbations. Magn Reson Med. 1995; 34:555–66. [PubMed: 8524024]
24. Dixon W. Simple proton spectroscopic imaging. Radiology. 1984; 153:189–194. [PubMed: 6089263]
25. Schäfer A, Wharton S, Gowland P, Bowtell R. Using magnetic field simulation to study susceptibility-related phase contrast in gradient echo MRI. Neuroimage. 2009; 48:126–37. DOI: 10.1016/j.neuroimage.2009.05.093 [PubMed: 19520176]
26. He X, Yablonskiy DA. Biophysical mechanisms of phase contrast in gradient echo MRI. 2009; 106
27. Duyn JH, Van Gelderen P, Li T, De Zwart JA, Koretsky AP, Fukunaga M. High-field MRI of brain cortical substructure based on signal phase. 2007
28. Fan AP, Bilgic B, Gagnon L, Witzel T, Bhat H, Rosen BR, Adalsteinsson E. Quantitative oxygenation venography from MRI phase. Magn Reson Med. 2013; 00:1–11. DOI: 10.1002/mrm.24918
29. Wells WM, Grimson WEL, Kikinis R, Jolesz FA. Adaptive Segmentation of MRI Data. 1996; 15
30. Donahue MJ, Lu H, Jones CK, Edden RaE, Pekar JJ, van Zijl PCM. Theoretical and experimental investigation of the VASO contrast mechanism. Magn Reson Med. 2006; 56:1261–73. DOI: 10.1002/mrm.21072 [PubMed: 17075857]
31. Yablonskiy, DA., Haacke, EM. Theory of NMR Signal Behavior in Magnetic ally Inhomogeneous Tissues : The Static Dephasing Regime.
32. Marques JP, Bowtell R. Application of a Fourier-based method for rapid calculation of field inhomogeneity due to spatial variation of magnetic susceptibility. Concepts Magn Reson Part B Magn Reson Eng. 2005; 25B:65–78. DOI: 10.1002/cmr.b.20034
33. Salomir R, de Senneville BD, Moonen CT. A fast calculation method for magnetic field inhomogeneity due to an arbitrary distribution of bulk susceptibility. Concepts Magn Reson. 2003; 19B:26–34. DOI: 10.1002/cmr.b.10083
34. Ong, F., Uecker, M., Tariq, U., Hsiao, A., Alley, MT., Vasanawala, SS., Lustig, M. Berkeley Advanced Reconstruction Toolbox. International Society for Magnetic Resonance in Medicine; 2015; Toronto, Canada. p. 2486
35. Jenkinson M, Pechaud M, Smith S. BET2 - MR-Based Estimation of Brain, Skull and Scalp Surfaces. Eleventh Annual Meeting of the Organization for Human Brain Mapping. 2005
36. Cusack R, Papadakis N. New Robust 3-D Phase Unwrapping Algorithms: Application to Magnetic Field Mapping and Undistorting Echoplanar Images. Neuroimage. 2002; 16:754–764. DOI: 10.1006/nimg.2002.1092 [PubMed: 12169259]
37. Schweser F, Deistung A, Lehr BW, Reichenbach JR. Quantitative imaging of intrinsic magnetic tissue properties using MRI signal phase: An approach to in vivo brain iron metabolism? Neuroimage. 2011; 54:2789–2807. DOI: 10.1016/j.neuroimage.2010.10.070 [PubMed: 21040794]
38. Bilgic, B. [Accessed 2014 Sept 1] Fast l1-Regularized QSM with Magnitude Weighting and SHARP background filtering [Internet]. c2014. Available from http://martinos.org/~berkin/Fast_QSM_Magnitude_Toolbox.zip

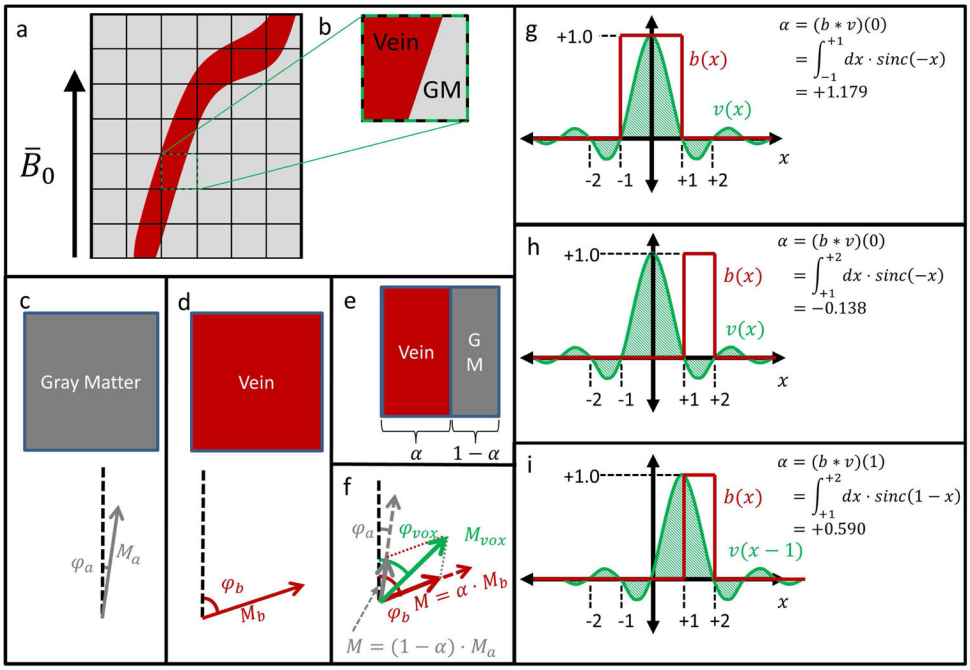

Figure 1.

(a) A small vessel relative to the acquisition voxel size will suffer from partial-volume effects. (b) Such a voxel with partial-volume effects overlays two distinct tissue regions: vein and parenchyma (eg gray matter). (c) A voxel containing entirely gray matter has a complex signal with magnitude M_a and phase φ_a. (d) A voxel containing entirely venous blood has a complex signal with magnitude M_b and phase φ_b. (e) A voxel containing regions of each tissue consists of a fraction α of blood, and a fraction $1 - \alpha$ of gray matter. (f) The partial-volume voxel signal will be the sum of the signals in (c) and (d) weighted by the fractions in (e). φ_a, φ_b, M_a, M_b, α, φ_{VOX}, and M_{VOX} are defined in Table 1. (g) Simplified 1D example where the vessel binary mask $b(x)$ coincides with the main lobe of the voxel function $v(x)$, and $\alpha > 1$. (h) 1D example where $b(x)$ coincides with a negative lobe of $v(x)$, and $\alpha < 0$. In (g) and (h), the different limits of integration represent the different spatial extents of the respective blood vessels. (i) For the same system as in (h), an adjacent voxel has positive α with a larger magnitude.

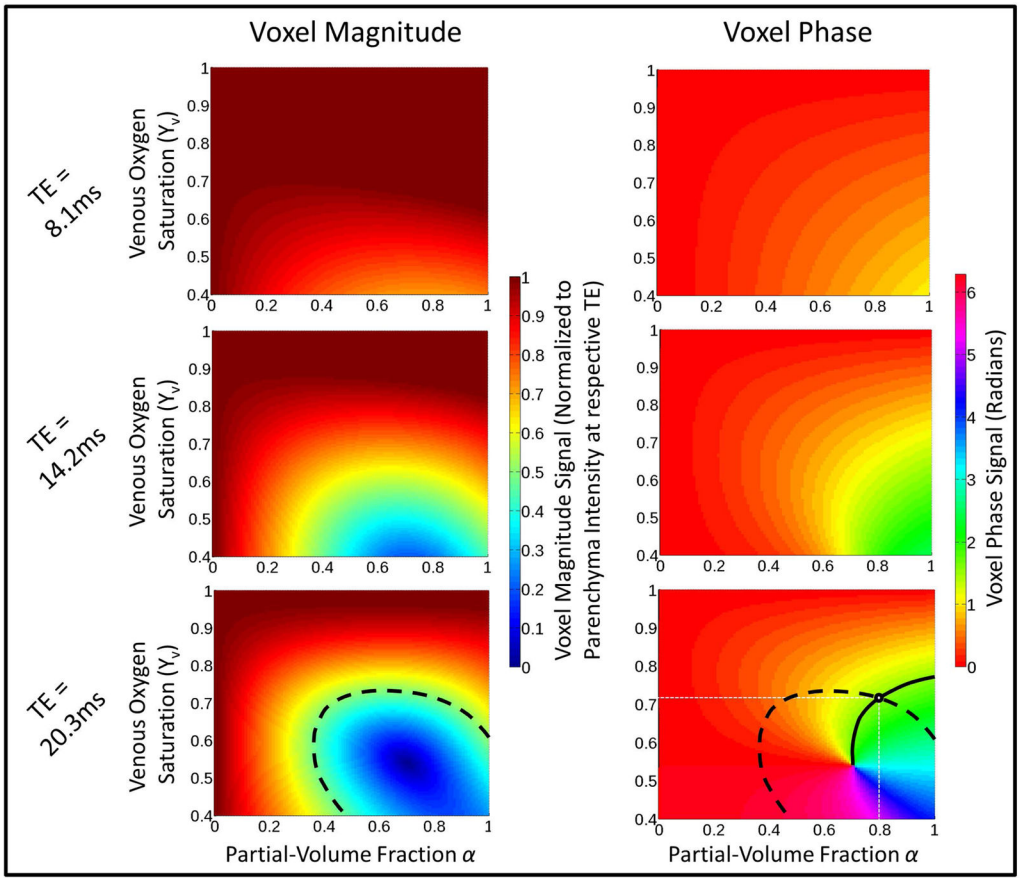

Figure 2.

Voxel magnitude intensity and signal phase for different percent hemoglobin oxygen saturation (Y_v) and partial-volume fraction (α) choices at TE of 8.1ms, 14.2ms, and 20.3ms. A voxel magnitude signal of 0.5 at TE=20.3ms is shown with the dashed line. This line illustrates the set of possible (α, Y_v) pairs that correspond this magnitude. Similarly, a phase measurement of 1.5 rad is shown by the solid line, and specifies a different set of possible (α, Y_v) pairs. The intersection of the two curves determines a single possible solution of (α = 0.78, Y_v = 0.715)

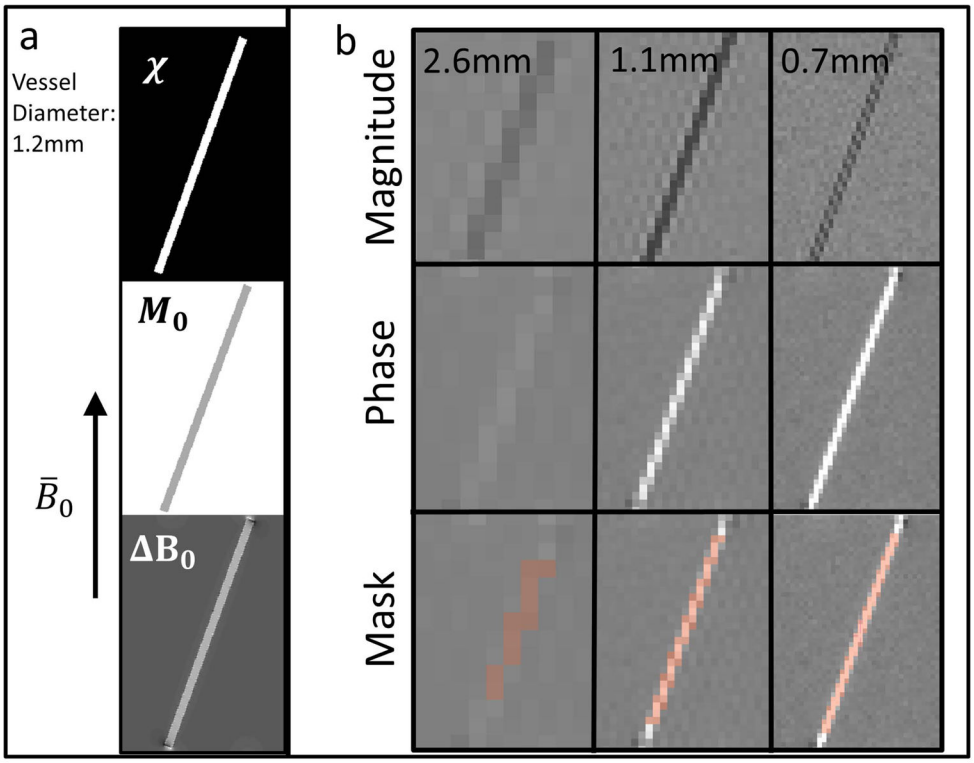

Figure 3.
(a) Susceptibility (χ), magnitude signal (M_0), and field perturbation (ΔB_0) maps used for simulation. (b) Representative simulated acquisitions at 2.6mm, 1.1mm and 0.7mm isotropic voxel size. The magnitude image, phase image, and vessel ROI mask are shown.

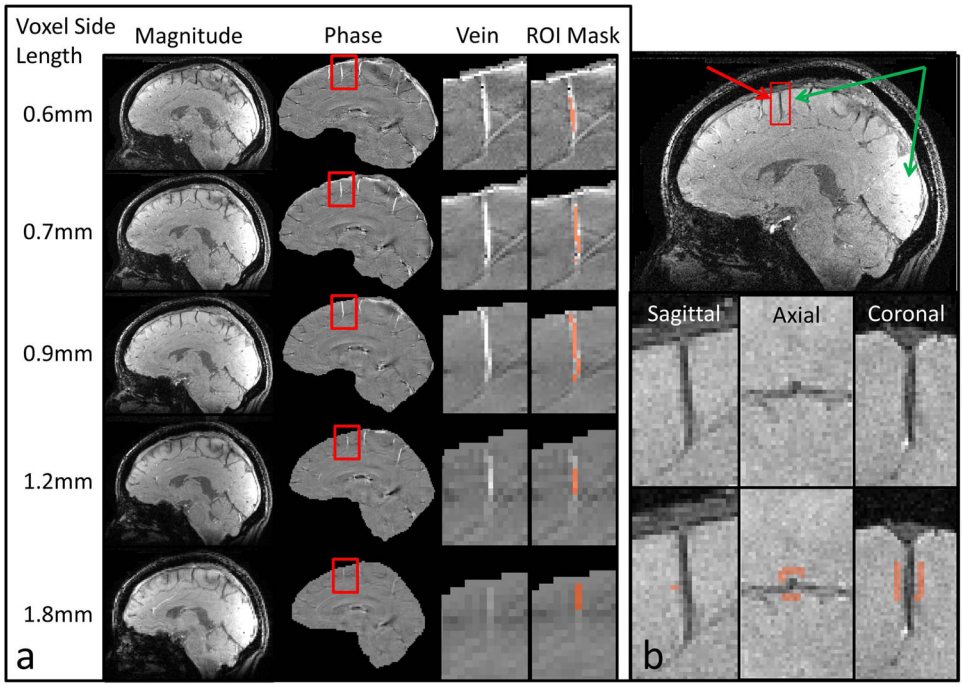

Figure 4.

(a) in vivo data acquired from one subject at all five native resolutions showing: GRE magnitude images; GRE phase images; Close-up of the phase image, centered on highlighted vein; Close-up showing vein ROI mask. (b) GRE magnitude image. Green arrows illustrate the signal variation due to inhomogeneous coil sensitivities. To estimate the background bias field, the signal is averaged over a rectangular gray matter ROI proximal to the vessel of interest.

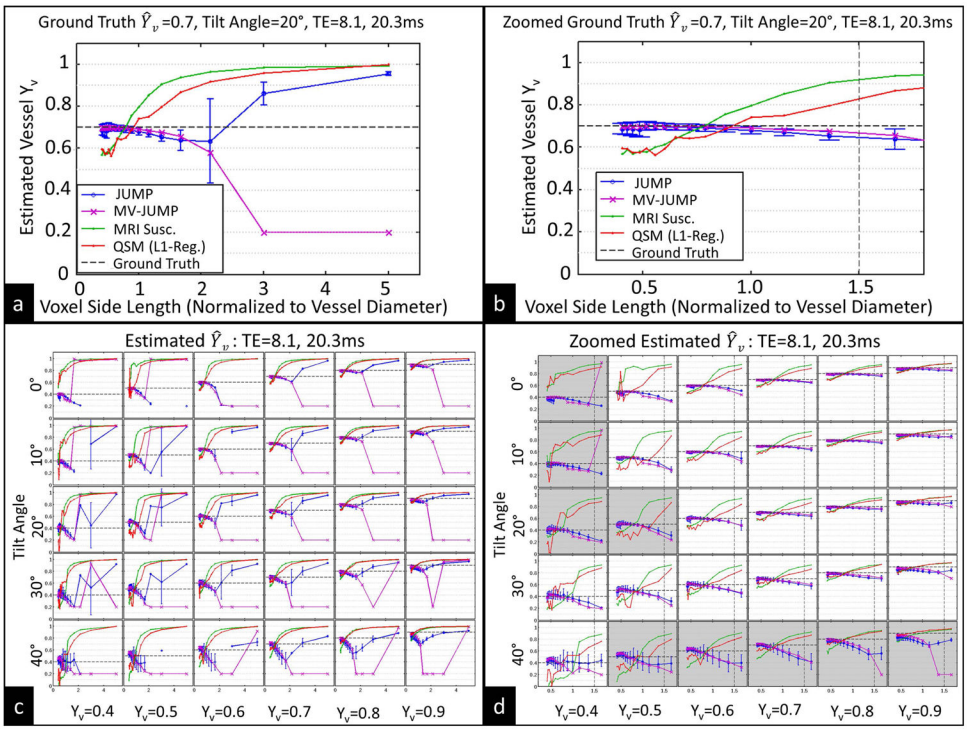

Figure 5.

Numerical vessel simulation results. (a) JUMP, MV-JUMP, MRI susceptometry, and QSM estimates of $\hat{Y}_V$ for Ground Truth Y_V=0.7, vessel angle=20°, for all resolutions. (b) Same data in (a), zoomed to shown only resolutions with voxel side length under 2x vessel diameter. (c) JUMP and MV-JUMP $\hat{Y}_V$ estimates for combinations of ground truth Y_V and vessel angle. (d) Same data in (c), zoomed to shown only resolutions with voxel side length under 2x vessel diameter. Vertical dashed line in (b) and (d) represents 1.8mm isotropic voxel size, the largest size used in in vivo experiments.

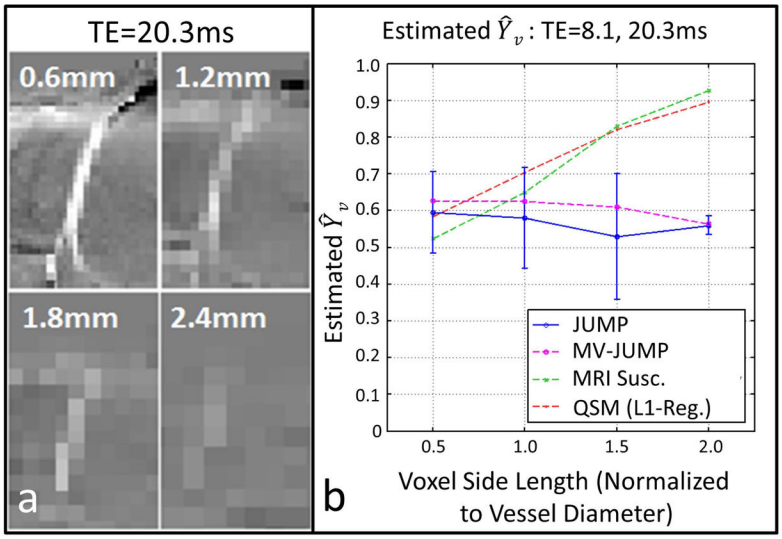

Figure 6.

(a) Zoomed view of pial vein measured at four simulated acquisition resolutions (b) Measured $\hat{Y}_V$ across simulated acquisition voxel size. Curves show measurements obtained with JUMP, MV-JUMP, MRI susceptometry, and QSM.

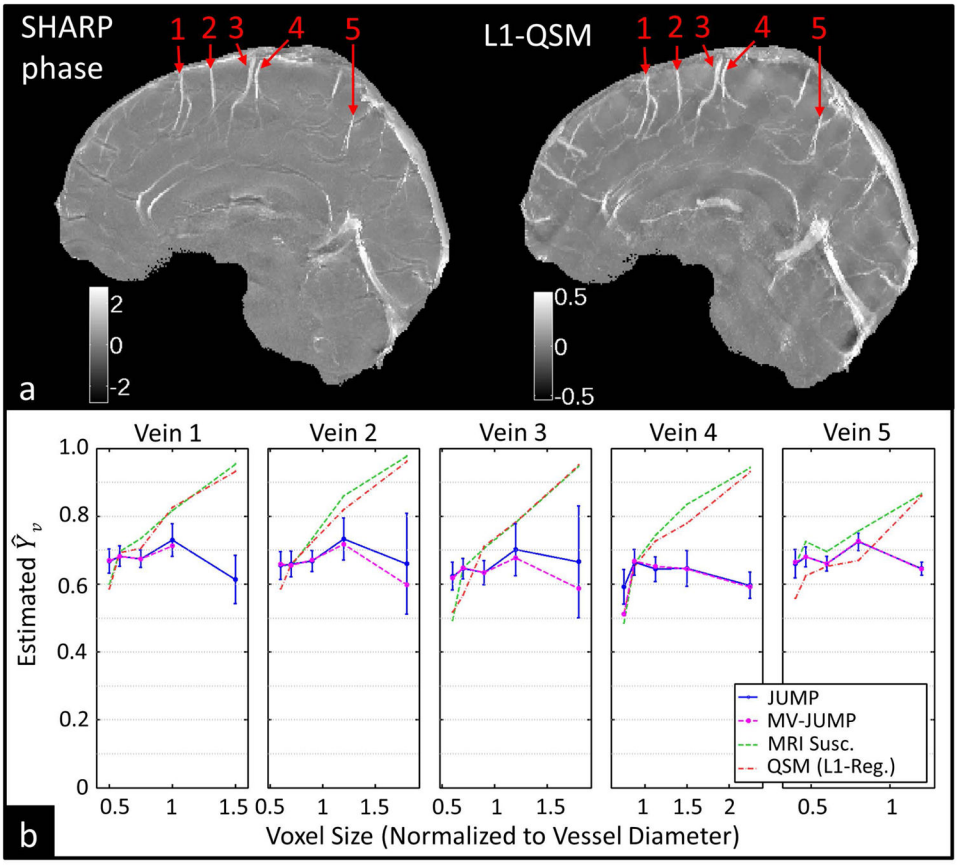

Figure 7.

$\hat{Y}_V$ results from subject 4 (a) Maximum-intensity projections of SHARP-processed phase images and L1-regularized QSM images showing measured pial veins. (b) $\hat{Y}_V$ measurements from JUMP, MV-JUMP, MRI susceptometry, and QSM plotted across acquisition resolution for all veins.

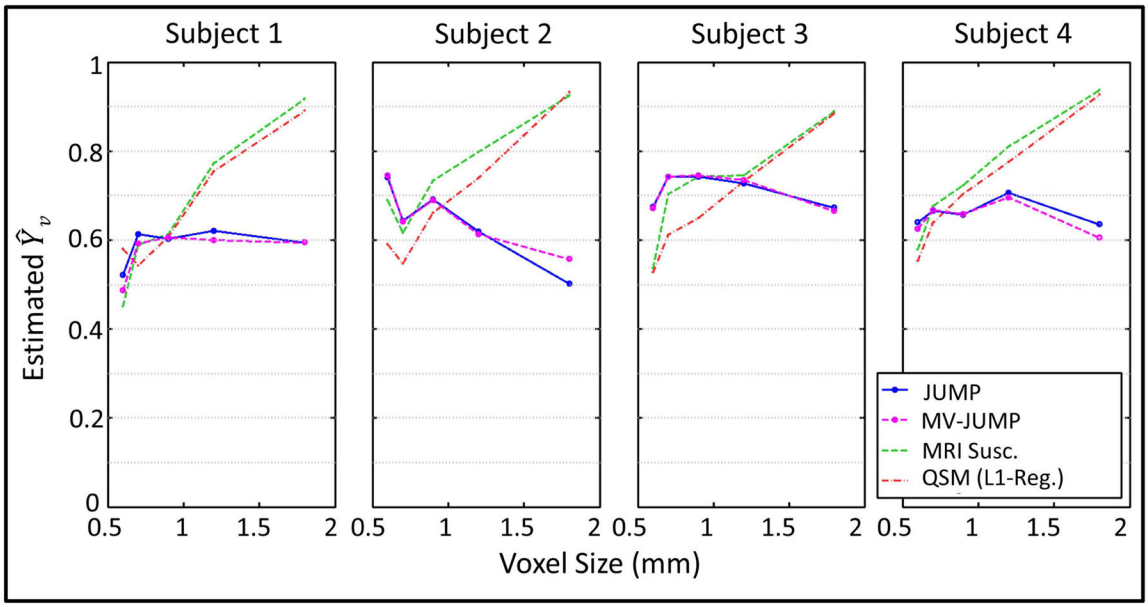

Figure 8.

5-vessel average $\hat{Y}_V$ measurements obtained with JUMP and MV-JUMP, shown for all subjects plotted against acquisition resolution.

Table 1

Two-compartment signal model parameters

Parameter	Physical Meaning	Known or Unknown?
α	Fraction of voxel comprised of vein (quantifies partial-volume effects)	Unknown model parameter
Y_v	Venous blood oxygenation	Unknown model parameter
φ_a	Spin phase in parenchyma compartment	Approximated as ≈ 0
φ_b	Spin phase in blood compartment	Function of Y_v and θ
M_a	Parenchyma signal magnitude	Known from signal model
M_b	Blood signal magnitude	Function of Y_v
K	Absolute signal intensity scale factor	Known from image
θ	Blood vessel tilt angle relative to B_0	Known from image
φ_{vox}	Voxel phase in acquired image	Known from image
M_{vox}	Voxel magnitude in acquired image	Known from image

Table 2

Single-vein $\hat{Y}_V$ results from subject 4; and 5-vein average $\hat{Y}_V$ from all subjects. Figures appended with an asterisk represent statistics computed from incomplete data.

		JUMP		MV-JUMP		MRI susceptometry		QSM	
		Y_v Range	**Δ_{Y_v}**	**Y_v Range**	**Δ_{Y_v}**	**Y_v Range**	**Δ_{Y_v}**	**Y_v Range**	**Δ_{Y_v}**
Subject 4, Single Vein	Vein 1	0.61 to 0.73	**0.12**	0.67 to 0.71	**0.04***	0.60 to 0.96	**0.36**	0.59 to 0.93	**0.34**
	Vein 2	0.66 to 0.73	**0.07**	0.60 to 0.72	**0.12**	0.65 to 0.98	**0.33**	0.59 to 0.96	**0.37**
	Vein 3	0.62 to 0.70	**0.08**	0.59 to 0.68	**0.09**	0.49 to 0.95	**0.46**	0.52 to 0.95	**0.43**
	Vein 4	0.59 to 0.66	**0.07**	0.51 to 0.67	**0.16**	0.49 to 0.94	**0.45**	0.52 to 0.93	**0.41**
	Vein 5	0.65 to 0.72	**0.07**	0.64 to 0.73	**0.09**	0.66 to 0.87	**0.21**	0.56 to 0.86	**0.30**
All Subjects, 5-vein average	Subject 1	0.52 to 0.62	**0.10**	0.49 to 0.61	**0.12**	0.45 to 0.92	**0.47**	0.54 to 0.89	**0.35**
	Subject 2	0.50 to 0.74	**0.24**	0.56 to 0.75	**0.19***	0.62 to 0.93	**0.31**	0.55 to 0.93	**0.38**
	Subject 3	0.67 to 0.74	**0.07**	0.67 to 0.75	**0.08***	0.54 to 0.89	**0.35**	0.53 to 0.89	**0.36**
	Subject 4	0.64 to 0.71	**0.07**	0.61 to 0.70	**0.09***	0.58 to 0.94	**0.36**	0.55 to 0.93	**0.38**